Slip analysis of the Kokoxili earthquake using terrain-change detection and regional earthquake data

Cara G. Schiek*
José M. Hurtado Jr.*
Department of Geological Sciences, University of Texas at El Paso, 500 W. University Ave., El Paso, Texas 79968, USA

ABSTRACT

The Kokoxili earthquake occurred on 14 November 2001 along the Kunlun fault. To analyze the type of deformation along several segments of the fault, this study employs Fourier transform terrain-change detection to detect horizontal pixel offsets between time-separated Advanced Spaceborne Thermal Emission and Reflection Radiometer (ASTER) satellite images. The results allow us to model the slip direction and amount of slip due to the earthquake. Three segments of the fault were analyzed, each with different strain kinematics. Our analysis detected left-lateral slip, a displacement of 311 m, and areas of transpression and transtension in the proximal area of the Kunlun fault. The image geodetic results are consistent with published field measurements and stress analysis using regional earthquake data. The combination of the field measurements, stress and strain analysis, and geodetic results displays patterns of deformation along the fault that are influenced by the fault's geometry. This study demonstrates for the first time the utility of ASTER optical satellite imagery for acquiring quantitative measurements of surface deformation.

Keywords: Kunlun fault, deformation, ASTER, Fourier analysis, Tibet.

INTRODUCTION

On 14 November 2001, the Kunlun fault experienced a M_w 7.8 earthquake, which became known as the Kokoxili earthquake. Since the earthquake, several studies have been conducted along the faulted region in order to describe the slip direction, amount of slip, deformational style, and principal stress orientations (Lin et

*Schiek—phone +1-915-747-5501, e-mail schiek@ geo.utep.edu; Hurtado—hurtado@geo.utep.edu.

al., 2002, 2003, 2004; Andronicos et al., 2004a, 2004b; Ozacar and Beck, 2004). In this study, we used terrain-change detection using satellite imagery to model slip along the rupture zone of the 2001 Kokoxili earthquake. The resulting vector displacement fields were then analyzed using a strain inversion algorithm in order to determine the principal extensional and shortening axes. We compared both the resulting displacement fields and the infinitesimal strain axes to the results of the previous studies in order to understand the pattern of deformation along the rupture zone. To first order, the deformation field is influenced by the fault's segmented geometry.

Kokoxili Earthquake

The Kokoxili earthquake created a 400-km-long surface rupture and as much as 16.3 m of left-lateral strike slip (Van der Woerd et al., 2002; Lin et al., 2002, 2003) (Fig. 1). This slip is most evident as fault scarps developed on alluvial fans and terraces (Table 1). Lin et al. (2003) divided the portion of the fault that slipped in 2001 into four segments based on morphological characteristics, geological structures, and displacement distributions (Fig. 1). The four segments are (from west to east): Buka Daban Peak, Hongshui River, Kusai, and Kunlun Pass. All segments exhibit sinistral displacement, but each segment also displays small amounts of either transtensional or transpressional deformation. For instance, the northern part of the Hongshui River segment displays a small transpressional component, which is manifested in mole tracks where the fault bends to the north (Lin et al., 2004). The Buka Daban Peak and Kusai segments both display transtension as indicated by the occurrence of many extensional cracks (Lin et al., 2003).

The field observations by Lin et al. (2003) are in agreement with a regional stress analysis by Andronicos et al. (2004a, 2004b). Their work used focal mechanisms for $M_w > 5.5$ earthquakes

from the Harvard Central Moment Tensor catalogue that occurred between 1977 and 2004. For each event, the trend and plunge of the axes of greatest (P) and least compression (T) were extracted and sorted into five categories: thrust, transpressive, strike slip, transtensive, and normal. When Andronicos et al.'s (2004a, 2004b) results are combined with the results from Lin et al. (2003), the deformation types observed along the fault correlate with the fault's segmented geometry (Fig. 1). For instance, Lin et al. (2003) observed tensional cracks and sinistral displacement (Table 1) in the Kusai segment north of Kusai Lake, and Andronicos et al. (2004a, 2004b) showed transtensive stresses north of the fault and strike slip south of the fault for that same segment (Fig. 1). This correlation is also depicted in an earthquake rupture model for the Kokoxili earthquake designed by Ozacar and Beck (2004), who used inverted teleseismic P waveforms, differing types of focal mechanisms (ranging from pure strike slip to strike slip with compressional and tensional components), and source models.

Terrain-Change Detection

The coseismic slip resulting from the Kokoxili earthquake can be measured with optical remote-sensing data. To do this, image processing algorithms are needed to measure apparent offsets in the geographic locations of corresponding pixels in two (or more) images of the same portion of Earth's surface taken at different times. These interimage pixel offsets define vectors with orientations that indicate the direction of terrain displacement and lengths that denote the magnitude of that displacement. Previous work with Satellite Probatoire d'Observation de la Terre (SPOT) images has shown the feasibility of using optical imagery for lateral displacement change detection using Fourier methods (Van Puymbroeck et al., 2000; Dominguez et al., 2003; Michel and Avouac, 2002; and Feigl et al., 2002). For example, Dominguez et al.
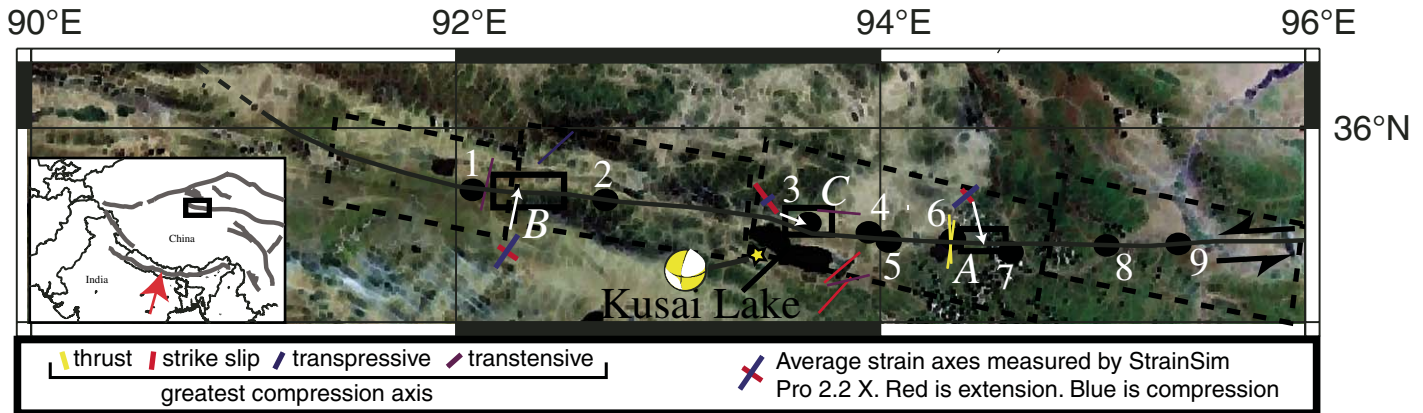
Figure 1. Location map. Boxed area in inset shows location of Kunlun fault in northern Tibet. The red arrow in the inset indicates the relative motion of the Indian plate (Tapponnier et al., 2001). Box A indicates area A, which is a deformational setting characterized by strike slip with some transpressional component (Lin et al., 2003, 2004; Andronicos et al., 2004a, 2004b). Box B denotes area B, which lies in an area of transpression (Lin et al., 2003). Box C is area C and denotes an area of transtension (Lin et al., 2003, 2004; Andronicos et al., 2004a, 2004b). The dashed boxes represent rupture zone segments as defined by Lin et al. (2002, 2003). From left to right these segments are: Buka Daban Peak, Hongshui River, Kusai, and Kunlun Pass. Sites where offsets were measured by Lin et al. (2002, 2003) are shown by solid circles (see also Table 2). The colored line segments show the greatest compressional axes and represent the incremental strain field based on earthquake focal mechanisms (Andronicos et al., 2004a, 2004b). The focal mechanism plotted near Kusai Lake is from the Harvard Centroid Moment Tensor Catalog.

(2003) were able to resolve a coseismic displacement of 5–11 m (11 m near the epicenter) along a major thrust fault associated with the 1999 Chi Chi earthquake in the Central Range of Taiwan with this approach.

Two types of pixel offsets exist: true and apparent. Apparent pixel offsets can originate from a variety of sources and are not related to terrain changes. These apparent pixel offsets can be caused by topography, the geometry of the imaging system, the attitude of the spacecraft, and image decorrelation due to seasonal or atmospheric effects. The sources of apparent pixel offset need to be quantified and their effects minimized in order to obtain a reliable terrain-change measurement. The most important apparent pixel offsets to minimize are those that arise from incomplete knowledge of the geometry of the imaging system. The effect of this type of apparent pixel offset is strongest in the distal areas of the examined region, which we discuss in the results section, but can be mitigated by using image pairs that have a maximum of 3° difference in look angle (Schiek, 2004; Van Puymbroeck et al., 2000).

DATA

Advanced Spaceborne Thermal Emission and Reflection Radiometer (ASTER) is a pushbroom instrument, which contains three separate imaging subsystems that cover the visible and near infrared spectrum (VNIR) with 15 m resolution, the shortwave infrared spectrum (SWIR) with 30 m resolution, and the thermal infrared spectrum (TIR) with 90 m resolution. The VNIR subsystem consists of a solid-state focal plane that records imagery one line at a time in a 60-km-wide swath as the satellite passes over Earth. It includes two Schmidt reflecting-refracting telescopes, both with a focal length of 329 mm. One telescope is nadir (straight down) looking, and the other points 27.6° off-nadir, allowing for stereo viewing and the extraction of digital elevation models (DEMs) (Abrams et al., 2002). All images used in this study are VNIR band 3n (0.78–0.86 μm wavelengths) images from ASTER level 1B scenes. This band was chosen because it has the highest resolution and because a sensor model (Yu et al., 2003), which describes the interior and exterior orientations of the imaging system (e.g., Mikhail et al., 2001), is available. ASTER level 1B scenes were chosen due to their availability in this region, and because they have already been preprocessed to remove some artifacts (i.e., stripe removal, but not parallax) and have been georeferenced. For more information about ASTER, refer to Abrams et al. (2002) or http://asterweb.jpl.nasa.gov/.

For three locations along the Kunlun fault, pairs of time-separated ASTER images were acquired (Fig. 1; Table 2). In the first, area A, we examined an image pair that spans the 2 yr time interval from March 2000 to July 2002. This area lies at the eastern end of the Kusai segment (Fig. 1; Table 2). The images we analyzed for area A show no well-defined fault scarps along the mapped trace of the Kunlun fault. Area B lies in the western part of the Hongshui River segment (Fig. 1; Table 2), and here we use images that cover a 2 mo interval from 4 November 2001 to 22 December 2001. Area C is located in the western part of the Kusai segment (Fig. 1; Table 2). The images acquired for area C span more than a year, from October 2000 to December 2001. The images used for both areas B and C include well-defined fault scarps that formed during the 2001 earthquake.

METHODS

Preprocessing and Image Registration Protocol

Our analysis required a series of image preprocessing steps. The goal of the preprocessing is to minimize apparent pixel offsets, thus enhancing the true pixel offset due to terrain change. The principal preprocessing step comprised orthorectification of the input imagery using the Yu et al. (2003) sensor model, image parameters found in the metadata of each input image, an shuttle radar topography mission (SRTM) DEM of the investigated area, and the Leica Photogrammetry Suite in ERDAS IMAGINE 8.7. See Table 2 for a summary of the image parameters and results of the orthorectification. The ground-control points (GCP) listed in Table 2 were chosen in areas outside of the faulted area, where no change is thought to have occurred. The Leica Photogrammetry Suite performs

orthorectification through a series of triangulation calculations between the DEM, image, and ground-control points. After the triangulation procedure, the image is given corrected coordinates, which are corrected for the curvature of the Earth, and which reflect the true geographic location of pixels. For details about the protocol used to complete our orthorectification, we refer the reader to Schiek (2004).

Our method requires that the input image pair is initially co-registered to within ±1 pixel. By linking the images using ENVI 4.0 software, and comparing the same geographic location in corresponding images, we were able to evaluate the quality of the orthorectification. Area A was the only set of images not to pass the ±1 pixel criterion. In this case, we then attempted to co-register them again using ENVI. The result of this co-registration also did not meet the ±1 pixel criterion. This poor co-registration is due to the large pointing-angle difference between the two images (Table 2). However, as seen in the results (Fig. 2), this image pair was still sufficient for producing a well-constrained displacement vector direction, but gave an unacceptable vector magnitude.

Fast Fourier Transform Change Detection (FFT_CD) Algorithm

By taking the Fourier transform of an image, it can be separated into its spatial frequency components. Our terrain-change analysis in the frequency domain examines the phase difference between the various frequency components of the two input images. In the spatial domain, this difference represents the sum of apparent and true pixel offsets, and is defined by:

$$f_2(x,y) = f_1(x - x_0, y - y_0), \qquad (1)$$

where f_1 (before image) and f_2 (after image) differ by a displacement (x_0, y_0) (Brown, 1992). In the frequency domain, the Fourier transformed images, F_1 and F_2, have the relationship:

$$F_2(\xi, \eta) = e^{-j2\pi(\xi \cdot x_0 + \eta \cdot y_0)} F_1(\xi, \eta), \qquad (2)$$

where ξ and η are the vertical and horizontal spatial frequencies, respectively, and j is $\sqrt{-1}$. Since the two Fourier transform images have the same magnitudes (i.e., amplitude or frequency), the only difference between them is in their phases, and that difference is directly related to the shift in the spatial domain, (x_0, y_0). The Fourier shift theorem gives us the relationship between the Fourier transforms of the shifted and nonshifted images (Brown, 1992):

$$\frac{\left[F_1(\xi, \eta) F_2^*(\xi, \eta) \right] * wl}{\left[\left| F_1(\xi, \eta) F_2^*(\xi, \eta) \right| \right] * wl} = e^{j2\pi(\xi \cdot x_0 + \eta \cdot y_0)}, \quad (3)$$

where F^* indicates the complex conjugate of F. The inverse Fourier transform of the right-hand side of equation 3 is an impulse function with a maximum at (x_0, y_0), the spatial shift between the two input images (Xie et al., 2003).

The term wl in equation 3 is a water-level deconvolution (Clayton and Wiggins, 1976):

$$wl = \frac{1}{\max(\Phi)}, \qquad (4)$$

where Φ is the first product in either the numerator or denominator of equation 3. This term is necessary in order to remove a low-frequency component present in the numerator and denominator of equation 3. This low-frequency component results from edge effects due to windowing, errors introduced by the user during

TABLE 1. SURVEYED DISPLACEMENTS FOR THE 2001 KOKOXILI EARTHQUAKE

Site	Displacement (m)	Offset feature	Observations
Segment 1: Buka Daban Peak			
1	4.5	Stream channel	Discontinuous shear zones
	4.4	Gully	Extensional horsetail cracks
	4.3	Gully	Mole tracks
Segment 2: Hongshui River			
2	4.8	Gully	Sinistral displacement
	4.6	Gully	Shear faults concentrated in narrow zones
			En echelon extensional cracks
Segment 3: Kusai Lake			
3	5.7	Alluvial fan	Distinct shear zones
	4	Gully	Extensional cracks
4	11.8	Terrace	Sinistral displacement
	16.3	Stream channel	Sand boils at site 6
	12.5	Alluvial fan	Mole tracks at site 7
5	13.5	Present-day moraine	
6	7.2	Stream channel	
7	4.5	Gully	
	4.3	Gully	
	3.8	Gully	
	6.8	Stream channel	
	3.3	Road	
Segment 4: Kunlun Pass			
8	4.2	Gully	Sinistral displacement
9	0.08	Gully	
	0.09	Gully	

Note: Data are from Lin et al. (2002, 2003, 2004).

TABLE 2. IMAGE PARAMETERS AND ORTHORECTIFICATION RESULTS

	Area A Kusai (east)		Area B Buka Daban Peak/ Hongshui River		Area C Kusai Lake (west)	
Image	March 2000	July 2002	Nov. 2001	Dec. 2001	Oct. 2000	Dec. 2001
Pointing angle (degrees)	−8.583	0.027	−2.832	−5.732	5.732	5.672
Pointing-angle difference (degrees)	−8.61		2.9		0.06	
Pixel difference before orthorectification	~100		4		~1	
Number of ground-control points	12	13	13	12	20	15
Root mean standard error (RMSE)	0.615	0.967	0.779	0.835	0.758	0.78
Pixel difference after orthorectification	~12		~1		0	
Fault scarp present	No		Yes		Yes	

preprocessing, and residual parallax resulting from incomplete knowledge of the attitude of the satellite. These effects need to be removed because they obscure the impulse function computed using equation 3. To remove the low-frequency component, equation 4 is applied whenever the following criterion is met:

$$\Phi(\xi,\eta) \geq 10^2 \cdot \left(mean(\Phi)\right) . \qquad (5)$$

The factor of 10^2 was determined empirically and maximized the performance of the water-level deconvolution as an adaptive filter.

Our methodology, as described so far, can only be used to detect full pixel shifts. Therefore, additional processing is needed. A subpixel shift measurement can be made by constructing a matrix composed of the eight neighbors surrounding the full pixel shift, (x_0, y_0). The maximum of these eight neighbors, (x_1, y_1), is then averaged with (x_0, y_0) (Gibson et al., 2001):

$$\left(|x_0,y_0|\right)^a + \left(|x_0,y_1|\right)^a = w_{x_1} , \qquad (6)$$

$$\left(|x_1,y_0|\right)^a + \left(|x_1,y_1|\right)^a = w_{x_2} , \qquad (7)$$

$$\left(|x_0,y_0|\right)^a + \left(|x_1,y_0|\right)^a = w_{y_1} , \qquad (8)$$

$$\left(|x_0,y_1|\right)^a + \left(|x_1,y_1|\right)^a = w_{y_2} , \qquad (9)$$

where a is an optimal value found empirically (Gibson et al., 2001), in this case $a = 0.65$, (x_0, y_1) and (x_1, y_0) are points adjacent to the two maxima, and $(w_{x_1}, w_{x_2}, w_{y_1}, w_{y_2})$ are weighting factors. Once the weighting factors are determined, the subpixel shifts in the x and y directions can be found by applying:
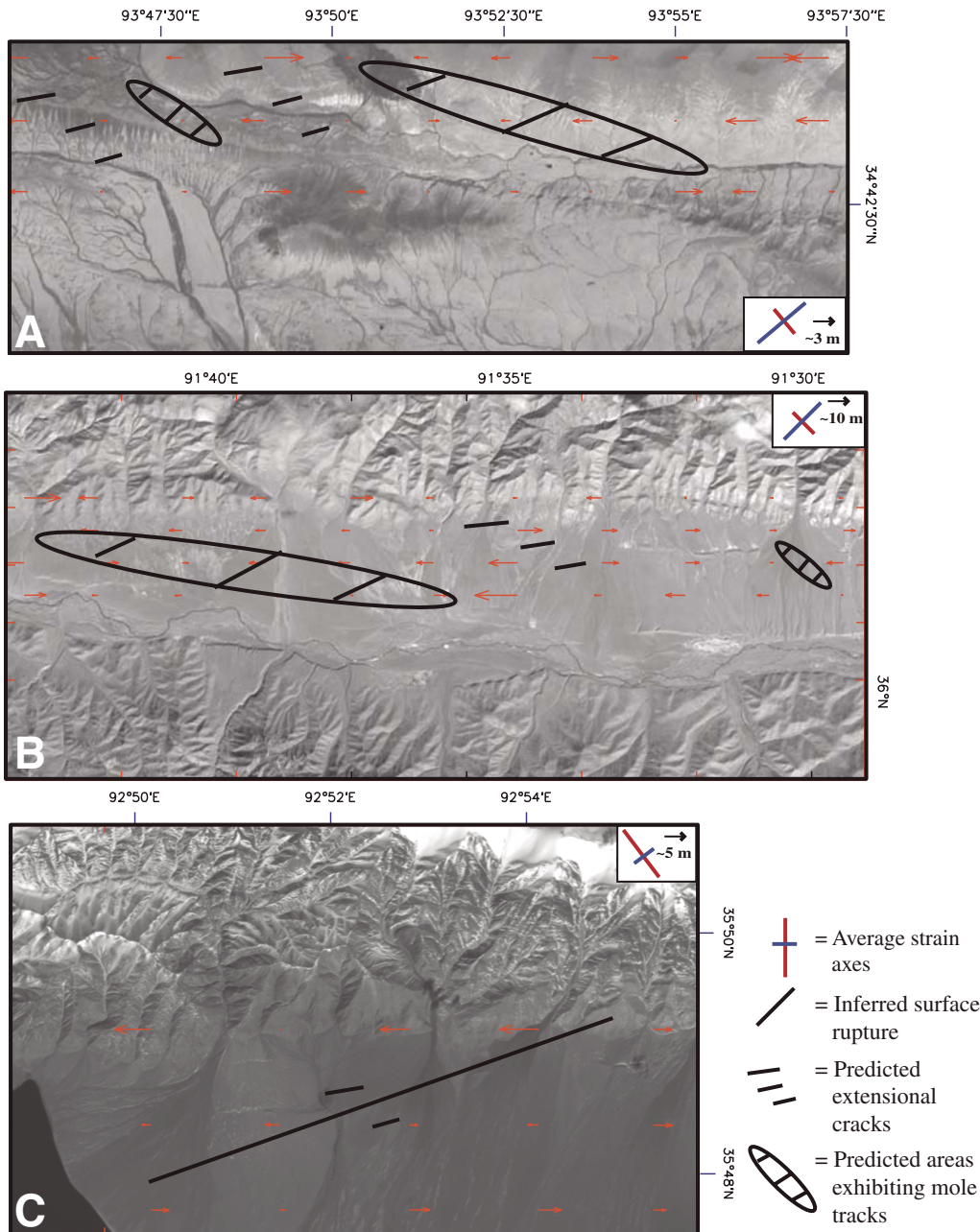

Figure 2. Terrain-change detection results for (A) area A, (B) area B, and (C) area C. The mapped structural features displayed on the vector maps are inferred from the strain inversion given in Figure 5. The red lines are the extensional axes, and the blue lines are the shortening axes. Vectors display magnitude and azimuth of slip.

$$\frac{\left[\left(w_{x_1} * x_0\right) + \left(w_{x_2} * x_1\right)\right]}{\left(w_{x_1} * w_{x_2}\right)} = \theta(x) \quad (10)$$

and

$$\frac{\left[\left(w_{y_1} * y_0\right) + \left(w_{y_2} * y_1\right)\right]}{\left(w_{y_1} * w_{y_2}\right)} = \theta(y), \quad (11)$$

where $\theta(x)$ and $\theta(y)$ are the subpixel shifts (Gibson et al., 2001). In the end, this method can resolve displacements on the order of 1/5 of the spatial resolution of the input images, or ~3.0 m for ASTER VNIR images.

A computer program, Fast Fourier Transform Change Detection (FFT_CD), was written to operate on the input images using a moving window scheme, computing a shift for each image segment. Each segment is analyzed separately and an aggregate pixel shift vector, indicating the direction and magnitude of terrain change for that region, is computed. Experimentation shows that the optimum window size is ~27 × 27 pixels (Schiek, 2004). The results of the FFT_CD analysis are depicted as pixel shift vectors overlain on the "before" image of the input image pair (Fig. 2). Figure 3 gives a direct comparison of the measurements made from this analysis to the measurements from the Lin et al. (2003) field measurements. The displacements and uncertainties we obtained are the average and standard deviation, respectively, of the magnitudes of the vectors in the vector map. The slip azimuth was obtained using rose diagrams (Fig. 4) and depicts the direction of slip along the fault. The azimuthal direction displaying the greatest population of vectors is considered to be the slip azimuth (Fig. 4). This slip direction is not to be confused with the direction of structural
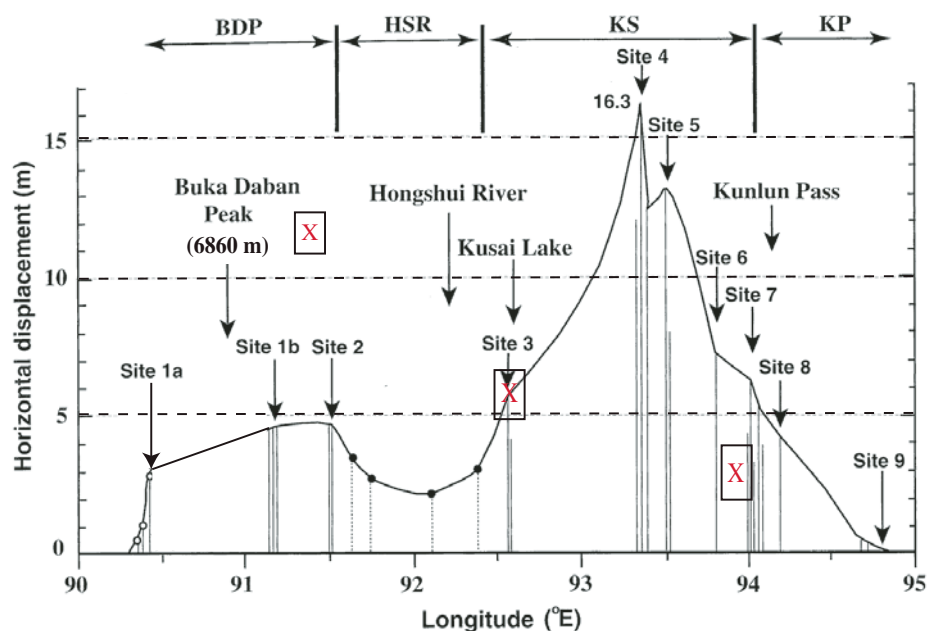

Figure 3. Comparison between the FFT_CD and Lin et al. (2003) left-lateral slip measurements. The black boxes with red X's represent measurements made using the FFT_CD method. The X represents the slip measurement, and the height of the box surrounding the X is 1σ uncertainty in that measurement. Open circles represent slip measured in the field by Lin et al. (2003) where the fault strikes between 90.3° and 90.5°. Closed circles represent slip measured by Lin et al. (2003) where the fault strikes between 91.5° and 92.5°. Acronyms are as follows: BDP—Buka Daban Peak segment; HSR—Hongshui River segment; KS—Kusai segment; and KP—Kunlun Pass. Figure is modified from Lin et al. (2003).

trends, such as mole tracks and extensional cracks. The structural trends occur ~45° from the measured slip azimuth (Fig. 2).

Strain Analysis

The resulting displacement fields were analyzed with a strain inversion program, StrainSim

Pro v. 2.5.7 (Allmendinger, 2005), to determine the strain field as well as the average strain axes responsible for the observed displacement field. We then compared each displacement field and corresponding strain field to the observations made by Lin et al. (2002, 2003) (Table 1) and the stress analysis by Andronicos et al. (2004a, 2004b) (Fig. 1). Figure 5 displays maps of strain
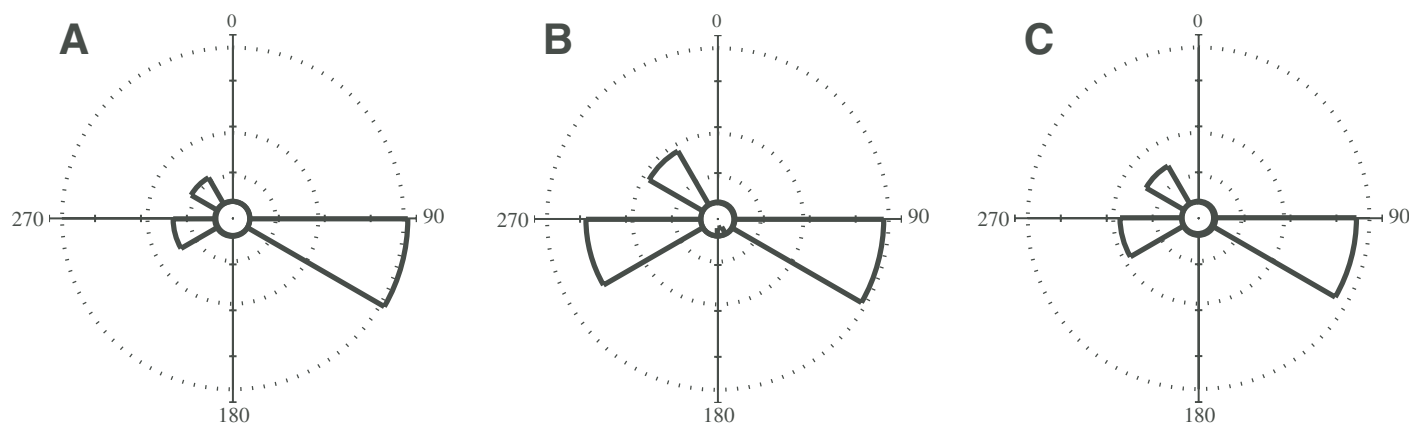

Figure 4. Rose diagrams displaying FFT_CD vector directions for (A) area A, (B) area B, and (C) area C.

axes calculated from StrainSim Pro 2.5.7 using the FFT_CD vector coordinates. These strain axes were used to map the structural trends displayed in Figure 2.

StrainSim Pro computes finite strain by importing a displacement field comprising the *x-y* coordinates of the vector starting points and their corresponding magnitudes (Fig. 2). The program creates two grids with this information. One uses the *x-y* coordinates as the initial position of pixels before deformation (red points in Fig. 5). The other grid is generated by using the magnitude values to compute vector end points, e.g., the final position of pixels after deforma-

tion (blue points in Fig. 5). A strain ellipse is computed by building a triangular irregular network (TIN) for both grids (Fig. 5) and comparing the two. After calculating the strain field, the average strain axes are determined by averaging the entire strain field.

RESULTS

All image pairs were processed using the FFT_CD algorithm to yield terrain-change vector maps (Fig. 2). Analysis of the area A image pair resulted in 2.91 ± 0.61 m of average left-lateral slip at an azimuth of 92° (Fig. 4A). The

sense of slip and azimuth of slip are consistent with Lin et al.'s (2002, 2003) results (Fig. 2A; Table 1). Assessing the accuracy of the amount of slip we obtained with FFT_CD in area A, however, is less straightforward. The closest of Lin et al.'s (2002, 2003) field sites is site 7 (Fig. 1; Table 1). They measured several offset features there that had displacements ranging from 3.3 m on a road to 6.8 m on a stream channel (Table 1). The first measurement of 3.3 m was, nevertheless, similar to our result. The underestimated amount of displacement in area A is likely due to the relatively poor quality of the orthorectification of the input imagery
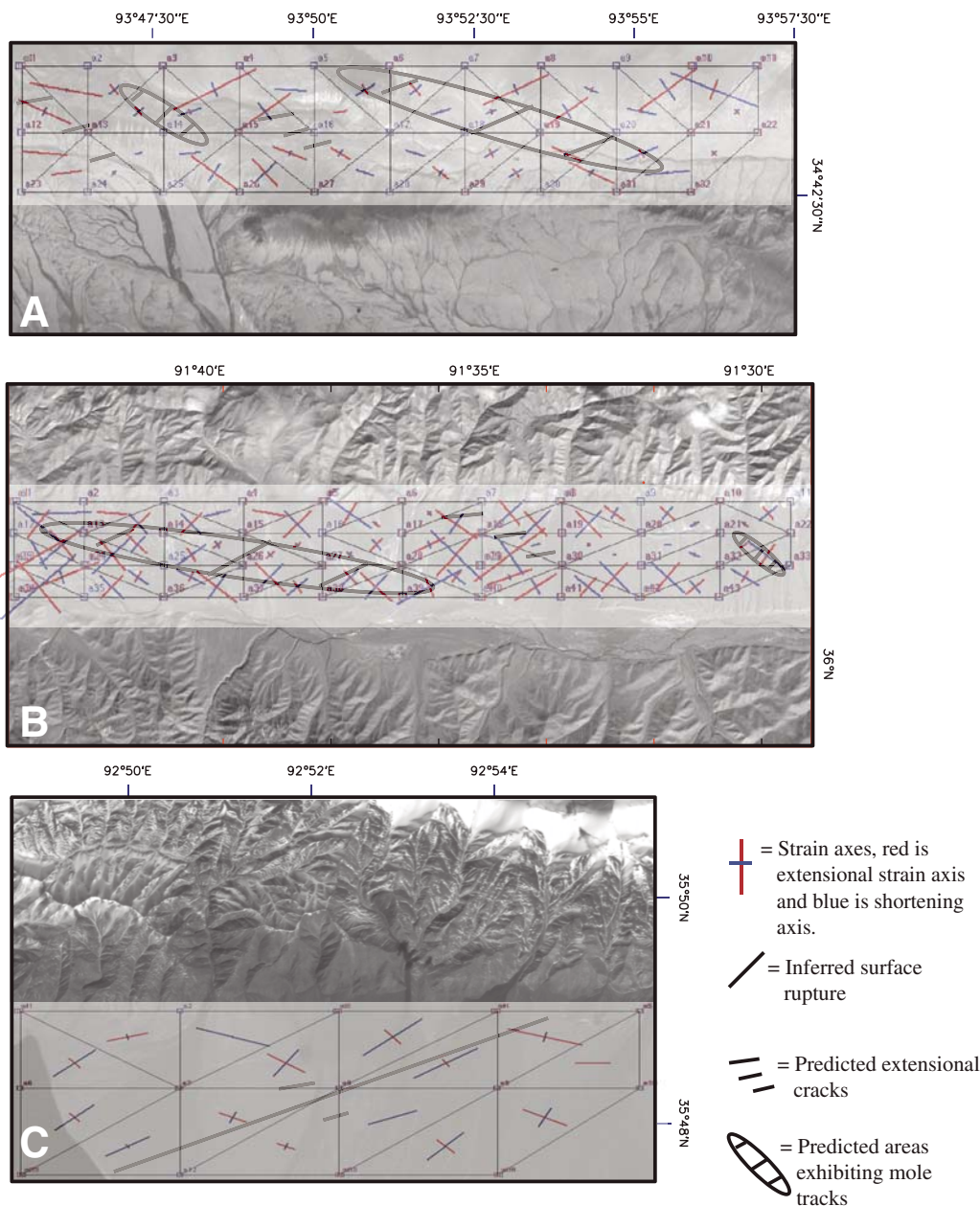

Figure 5. Strain analysis results for (A) area A, (B) area B, and (C) area C. Red lines indicate extension, and blue lines indicate compression. Red points are the fixed starting points of the vectors in Figure 2. Blue points are the displaced points (vector end points) calculated using the FFT_CD analysis. Triangles tying individual points together are the TIN (triangular irregular network) constructed by StrainSim Pro.

= Strain axes, red is extensional strain axis and blue is shortening axis.

= Inferred surface rupture

= Predicted extensional cracks

= Predicted areas exhibiting mole tracks

(Table 2); however, the azimuth of the displacement seems well constrained.

The average strain field in area A is compressional, and the strain ellipse has an extensional direction of 140° and a shortening direction of 50° (Figs. 2A and 5A). The compressional strain field measured for this area is compatible with the thrust-type greatest compression axes computed from earthquake data by Andronicos et al. (2004a, 2004b) (Fig. 1). In detail, we find the strain field for area A to be a complex pattern of extension and shortening (Fig. 5A). This complex pattern is compatible with the field observations of Lin et al. (2002, 2003) within the eastern Kusai Lake segment (e.g., site 7 in Table 1 and Fig. 1). For example, at site 7, located to the east of area A, Lin et al. (2002, 2003) observed mole tracks, which are indicative of compression. Our analysis predicts compression, and, therefore, features such as mole tracks, in this same area (Figs. 2A and 5A).

The investigation of area B obtained an average left-lateral displacement of 11.39 ± 0.56 m at an azimuth of 93° (Fig. 4B). The strain inversion yielded a compressional strain field with an extensional axis orientation of 125° and a shortening direction of 35° (Figs. 2B and 5B). Our measured displacement was much greater than the 4.6–4.8 m of displacement measured in a gully by Lin et al. (2002, 2003) (site 2 in Table 1; Fig. 1). Our overestimation of the amount of slip is mostly likely because the FFT_CD analysis considers a large swath (~30 km wide; Fig. 2B) surrounding the fault zone and not just the proximal area of the fault where Lin et al. (2002, 2003) conducted their field survey. Thus, our estimate includes both displacement along the fault, as well as displacement at some distance away from the fault (Fig. 2B).

Overall, area B displays transpression along the rupture zone, which is consistent with the transpressional state of stress obtained from the analysis of earthquake data (Fig. 1) (Andronicos et al., 2004a, 2004b). In detail, a complex distribution of compression and extension is observed in our results for area B (Fig. 5B). This complexity is borne out by field observations in the eastern Buka Daban River and western Hongshui River segments (sites 1 and 2 in Table 1 and Fig. 1) (Lin et al., 2002, 2003). In these areas, a variety of features are reported, including mole tracks, extensional cracks, and discontinuous shear zones (Lin et al., 2003).

The terrain-change analysis of the area C imagery detects sinistral slip along an azimuth of 92° (Fig. 4C). The resulting strain field is extensional, and the average strain ellipse has an extensional direction of 128° and a shortening direction of 37° (Figs. 2C and 5C). Extension is expected given the extensional cracks observed

in the field at site 3 (Table 1) (Lin et al., 2002, 2003) and the earthquake-derived extensional stress orientations (Fig. 1) (Andronicos et al., 2004a, 2004b). The average amount of slip obtained from our analysis, 6.18 ± 0.6 m, correlates well with the 5.7 m of displacement on an extensional crack measured by Lin et al. (2002, 2003) (site 3 in Table 2; Fig. 1).

DISCUSSION

The Fourier terrain-change detection and strain analysis successfully detected the slip from the 2001 Kokoxili earthquake. Here, we interpret our results in terms of large-scale and small-scale processes along the Kunlun fault. The large-scale observations explain the relationship between the relative plate motion of the India-Asia collision zone and the Kunlun fault. The small-scale observations may give insight into the surface rupture characteristics of the Kunlun fault.

The motion of India with respect to Asia in the Tibetan-Himalayan collision zone is at an azimuth of N15°E, which causes SW-NE compression in the Tibetan Plateau (Fig. 1). According to Tapponnier et al. (2001), the material in the plateau is extruded to the southeast along left-lateral faults, such as the Kunlun fault, in response to the collision. The SW-NE compressional direction and the SE extensional direction match the average strain axes we computed in our strain analysis (Fig. 2). We obtained an azimuth range of 35°–50° for the compressional direction and an azimuth range of 125°–140° for the extensional direction (Fig. 2). The computed compressional and extensional axes are similar to the overall stress field of the Tibetan-Himalayan collision zone, but the range of the computed numbers for compression and extension gives insight into stress changes along the Kunlun fault.

Although we detected terrain change consistent with left-lateral strike slip in all portions of the Kunlun fault that we studied, our results from areas A and C suggest that the Kunlun fault becomes more compressional toward the west. This is likely due to the northward bend the Kunlun fault takes, which strikes between 91.5° and 92.5° (Fig. 1) (Lin et al., 2003; Ozacar and Beck, 2004). This change in strike, in the face of the large-scale plate motion, results in variations in the state of stress at different sections along the fault. As the fault bends northward, the strain axes are rotated northward causing the compressional axes to be almost perpendicular to the fault. For instance, in area A, at the easternmost end of the study area where the fault strikes at 91.5°, the extensional direction is 140°, and the compressional direction is 50° (Figs. 1 and 2A).

By contrast, area B, located in the westernmost part of the study area, has an extensional direction of 125° and a compressional direction of 35° (Figs. 1 and 2B). However, the fault strikes at 92.5° through this area, and the more northward strike and the counterclockwise rotation of the stress axes yield a more transpressive regime in area B than in area A.

This transition to progressively more compressional stress along the Kunlun fault as a result of the change in strike and the rotation of the stress field is also manifested in the topography. In the eastern part of the study region, where areas A and C are located, the fault lies on the northern edge of a wide basin (Fig. 1). This basin becomes narrower to the west, terminating ~250 km to the west of area B, where the terrain becomes significantly more mountainous. The change in strike of the Kunlun fault has developed a very large-scale, northward restraining bend, which is evident in the transition from transpressive strike slip at the longitude of area B to the fold-and-thrust belt defined by the north Kunlun thrust system in the Kunlun Shan further west (Figs. 1 and 2; Table 1).

In detail, however, our results show complexity in the deformation patterns along the Kunlun fault not attributable to the northward bend alone. For instance, in area C, in between the transpressive zones at A and B, we observe strike slip with a significant transtensional component (Figs. 1, 2, and 5). In addition, along-strike variations in the magnitudes and orientations of the stress axes within areas A, B, and C show similar complexity (Figs. 1, 2, and 5). As with many large strike-slip faults, the surface expression of the Kunlun fault zone likely is composed of a series of en echelon strands (Lin et al., 2004), and compressional and tensional features can develop between and along these en echelon faults. Stepwise en echelon faulting is consistent with the field observations of Lin et al. (2003), who observed features such as mole tracks and extensional cracks (Table 1). Mole tracks occur between, and perpendicular to, right-stepping en echelon faults and strike N50°W (Figs. 2, 5, and 6) (Lin et al., 2003, 2004). This orientation is consistent with our inferred slip azimuth, and is also what is expected from Andronicos et al.'s (2004a, 2004b) stress orientations and our derived strain orientations. Similarly, extensional cracks occur along, and perpendicular to, the left-stepping en echelon faults and strike N40°W (Figs. 2, 5, and 6). From the calculated stress field in Figure 5, the predicted structural trends of mole tracks and extensional tracks is shown in Figures 2 and 5. Mole tracks will exist in areas where the compressional axis (blue) is greater than the extensional axis (red) (Fig. 5), and extensional cracks exist where the
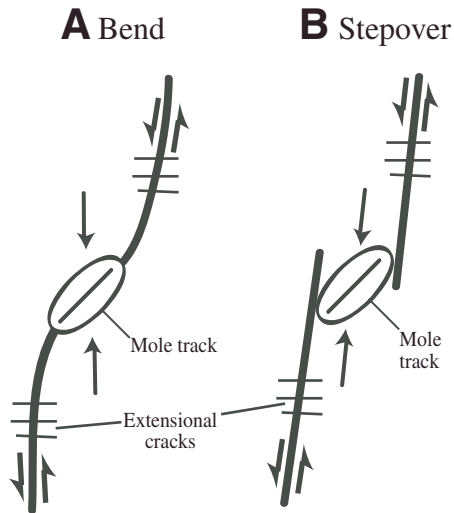
A Bend **B** Stepover

Figure 6. Schematic showing how compressional and extensional features develop along a left-lateral strike-slip fault comprising a series of en echelon steps. Right steps produce compression, resulting in mole tracks. Left steps produce extension, making extensional cracks

compressional axis (blue) is less than the extensional axis (red) (Fig. 5). If the two axes are equal, then strike-slip movement is expected. Figure 6 demonstrates how these features can exist between, and along, the right- and left-stepping en echelon fault strands.

CONCLUSION

The results from this study employing FFT_CD are consistent with the results of other studies conducted along the Kunlun fault (i.e., Lin et al., 2002, 2003; Andronicos et al., 2004a, 2004b). The observed pattern of increasing transpression to the west, with small pockets of transtension along the northward bend, is explained by the segmented geometry of the

Kunlun fault. Our technique offers a way to observe deformation along a fault in remote areas, such as the Kunlun fault, where other geodetic data may not be available. To achieve higher accuracy and precision in future studies, higher-resolution imagery, with more accurate orbital parameters, is necessary. The greater resolution will enable the FFT_CD procedure to measure smaller amounts of terrain change over smaller time intervals. More precise orbital parameters will greatly diminish uncertainties in the computed terrain-change vector maps, and increase the signal-to-noise ratio between true and apparent terrain change in a scene.

REFERENCES CITED

Abrams, M., Hook, S., and Ramachandran, B., 2002, ASTER user handbook (version 2): Pasadena, California, National Aeronautics and Space Administration (NASA) Jet Propulsion Laboratory, 135 p.
Allmendinger, R.W., 2005, StrainSimPro (version 2.5.7): Journal of Geological Education, v. 34, p. 191–195.
Andronicos, C.L., Velasco, A.A., and Hurtado, J.M., Jr., 2004a, Crustal flow in the India-Asia collision constrained by earthquakes: Eos (Transactions, American Geophysical Union), v. 85, no. 47, abstract T53D-07.
Andronicos, C.L., Velasco, A.A., and Hurtado, J.M., Jr., 2004b, Large-scale deformation in the India-Asia collision constrained by earthquakes and topography: Geological Society of America Abstracts with Programs, v. 36, no. 5, p. 483.
Brown, L.G., 1992, A survey of image registration techniques: AMC Computing Surveys, v. 24, no. 4, p. 325–376, doi: 10.1145/146370.146374.
Clayton, R.W., and Wiggins, R.A., 1976, Source shape estimation and deconvolution of teleseismic body waves: Geophysical Journal of the Royal Astronomy Society, v. 47, p. 151–177.
Dominguez, S., Avouac, J.-P., and Michel, R., 2003, Horizontal coseismic deformation of the 1999 Chi-Chi earthquake measured from SPOT satellite images: Implications for the seismic cycle along the western foothills of central Taiwan: Journal of Geophysical Research, v. 108, no. B2, p. 2083, doi: 10.1029/2001JB000951.
Feigl, K.L., Sarti, F., Vadon, H., McClusky, S., Ergintav, S., Durand, P., Burgmann, R., Rigo, A., Massonnet, D., and Reilinger, R., 2002, Estimating slip distribution for the Izmit mainshock from coeseismic GPS, ERS-1, RADARSAT, and SPOT measurements: Bulletin

of the Seismological Society of America, v. 92, no. 1, p. 138–160, doi: 10.1785/0120000830.
Gibson, S., Kreinovich, V., Longre, L., Penn, B.S., and Starks, S.A., 2001, Intelligent mining in image databases, with applications to satellite imaging and to Web search, in Kandel, A., Bunke, H., and Last, M., eds., Data mining and computational intelligence: Berlin, Springer-Verlag, p. 309–336.
Lin, A., Fu, B., Guo, J., Qingli, Z., Guangming, D., He, W., and Zhao, Y., 2002, Co-seismic strike-slip and rupture length produced by the 2001 M$_s$ 8.1 central Kunlun earthquake: Science, v. 296, no. 5575, p. 2015–2017, doi: 10.1126/science.1070879.
Lin, A., Masayuki, K., and Bihong, F., 2003, Rupture segmentation and process of the Mw 7.8 central Kunlun, China, earthquake: Bulletin of the Seismological Society of America, v. 93, no. 6, p. 2477–2492, doi: 10.1785/0120020179.
Lin, A., Guo, J., and Bihong, F., 2004, Co-seismic mole track structures produced by the 2001 Ms 8.1 central Kunlun earthquake, China: Journal of Structural Geology, v. 26, p. 1511–1519, doi: 10.1016/j.jsg.2004.01.005.
Michel, R., and Avouac, J.-P., 2002, Deformation due to the 17 August 1999 Izmit, Turkey, earthquake measured from SPOT images: Journal of Geophysical Research, v. 107, no. B4, doi: 10.1029/2000JB000102.
Mikhail, E.M., Bethel, J.S., and McGlone, J.M., 2001, Introduction to modern photogrammetry: New York, John Wiley & Sons, Inc., p. 23–27.
Ozacar, A.A., and Beck, S.L., 2004, The 2002 Denali fault and 2001 Kunlun fault earthquakes: Complex rupture processes of two large strike-slip events: Bulletin of the Seismological Society of America, v. 94, no. 6B, p. S278–S292, doi: 10.1785/0120040604.
Schiek, C.G., 2004, Terrain change detection using ASTER optical satellite imagery along the Kunlun fault, Tibet [M.S. thesis]: El Paso, Texas, University of Texas at El Paso, 101 p.
Tapponnier, P., Zhiqin, X., Roger, F., Meyer, B., Arnaud, N., Wittlinger, G., and Jingsui, Y., 2001, Oblique stepwise rise and growth of the Tibet Plateau: Science, v. 294, p. 1671–1677, doi: 10.1126/science.105978.
Van der Woerd, J., Meriaux, A.-S., Klinger, Y., Ryerson, F.J., Gaudemer, Y., and Tapponnier, P., 2002, The 14 November 2001, Mw = 7.8 Kokoxili earthquake in northern Tibet (Qinghai Province, China): Seismological Research Letters, v. 73, no. 2, p. 125–135.
Van Puymbroeck, N., Michel, R., Binet, R., Avouac, J.-P., and Taboury, J., 2000, Measuring earthquakes from optical satellite images: Applied Optics, v. 39, no. 20, p. 3486–3494.
Xie, H., Hicks, N., Keller, G.R., Huang, H., and Kreinovich, V., 2003, An IDL/ENVI implementation of the FFT based algorithm for automatic image registration: Journal of Computers and Geosciences, v. 29, p. 1045–1055, doi: 10.1016/S0098-3004(03)00104-3.
Yu, J., Cowgill, E., and Healy, S., 2003, Digital stereomapping in Imagine Orthobase: Pasadena, California, California Institute of Technology, p. 1–10.